Chapter 3

Classical Flare Models and New *RHESSI* Observations: The 2003-11-03 X3.9 Flare[1]

3.1 Introduction

Since its launch *RHESSI* has observed several X-class flares and thousands of mid-class and small flares. The compactness of microflares limits our access to details of the energy release and particle acceleration processes (Krucker et al., 2002). On the other hand, large and well-resolved flares usually involve multiple loops with complex structures, and the looptop (LT) and associated footpoint (FP) sources are not readily identified and separated (Gallagher et al., 2002; Lin et al., 2003). This makes a direct comparison of theoretical models with observations a challenging task (Alexander & Metcalf, 2002; Sui et al., 2002). This task would be easier for a large flare with a simple morphology, where one can identify source positions and evolutions with certainty (Tsuneta, 1996; Tsuneta et al., 1997).

In late October and early November of 2003, *RHESSI* and other instruments observed a series of X-class flares from solar Active Regions 0486 and 0488 (reminiscence of the 1991 June flares of the previous solar cycle; Schmieder et al., 1994). Among these flares, we studied an event that occurred on November 3 in AR 0488 at heliographic coordinate N09°, W77°. Unlike other X-class flares, e.g., the 2002 April 21 flare (Gallagher et al., 2002) and the gamma-ray flare on 2002 July 23 (Lin et al., 2003), this flare shows a surprisingly simple morphology with well-defined one LT and two FP sources.

In this chapter we present a brief description of the spatial evolution of the various emission regions of this flare. As we show, this provides an excellent example of the classical solar flare model of magnetic reconnection and energy release in an inverted Y magnetic field configuration (Kopp & Pneuman, 1976; Forbes & Acton, 1996; Aschwanden, 2002), whereby reconnection in the oppositely directed field lines leads to particle acceleration near the LT. The energy release and particle acceleration processes are not well understood; nevertheless, it is expected that the reconnection will produce closed loops at lower altitudes first and progress to higher overlying loops as time advances. Consequently, the altitude of the LT

[1]The majority of the material in this chapter was published in Liu, W., Jiang, Liu, & Petrosian (2004a).

source and the separation of the two FPs should increase with time. The flare studied here shows this exact behavior.

On the other hand, we also see evidence for deviations from the simplest reconnection models. Our study indicates that the reconnecting fields could be nonuniform and may have a shearing component. In the next section, we present the observations, data analysis, and our results. Their implications are discussed in § 3.3.

3.2 Observations and Data Analysis

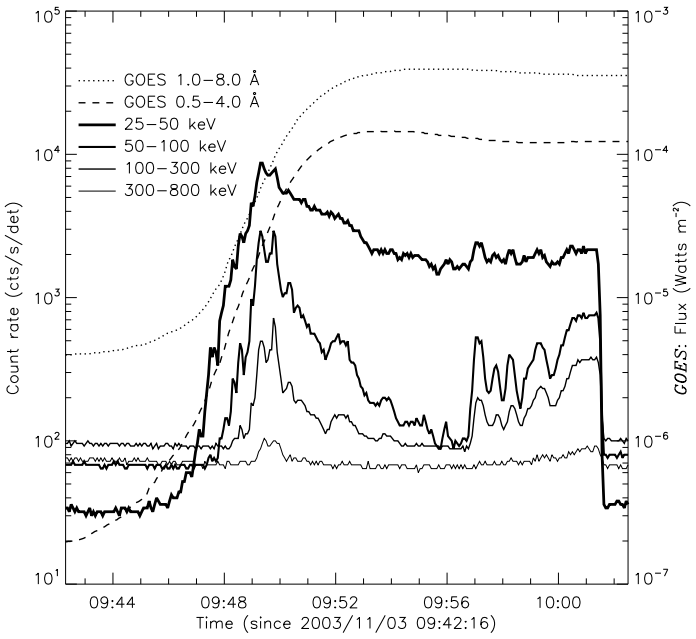

Figure 3.1: *RHESSI* count rates (counts/second/detector, averaged over 4 s intervals) and *GOES*-12 fluxes (in a 3 s cadence).

The flare under study, classified as a *GOES* X3.9-class flare, was observed by *RHESSI*, *Solar and Heliospheric Observatory* (*SOHO*), etc. Figure 3.1 shows the *RHESSI* and *GOES-12* light curves. In lower energy channels (< 25 keV), the count rates started to rise at around 09:43 UT, peaked about nine minutes later, and then began a monotonic declining phase until 10:01:20 UT when *RHESSI* entered the Earth's night region. The higher energy channel (> 50 keV) light curves exhibit two broad impulsive bursts, each of them consisting of several pulses with a more quiescent part in between, suggesting a persistent but episodic energy release process. Impulsive radio activities were also observed by the Nançay Observatory (Dauphin et al., 2006) A partial halo coronal mass ejection (CME) with a speed of ~ 1375 km s^{-1} was observed by the Large Angle and Spectrometric Coronagraph on *SOHO*.

3.2.1 Source Structure and Motion

To study the hard X-ray (HXR) source motion and structure, we obtained images at different energies in 20 s intervals from 09:46:20 through 10:01:00 UT using the CLEAN algorithm (Hurford et al., 2002) and front segments of detectors 3–8 to achieve a FWHM of $9\farcs8$ with a $0\farcs5$ pixel size. Figure 3.2 shows the HXR emission contours during the two main activity peaks. There are three sources: an LT, a northern FP (N-FP), and a southern FP (S-FP). The LT source dominates at low energies while the FPs dominate at high energies. As evident from the background pre-flare magnetogram obtained with the Michelson Doppler Imager (MDI), the N-FP is around a negative magnetic polarity region while the S-FP remains in a region of positive polarity. Note that early in the event there is a partial overlap between the N-FP and the LT source. Grids with higher spatial resolution will not help for this flare because grid 2 is in a severely degraded condition (Smith et al., 2002) and grid 1 will overresolve the sources (see Schmahl & Hurford, 2003, for technical details). A postflare (10:35:43 UT) EUV Imaging Telescope (EIT) 195 Å image (not shown) shows a loop structure that agrees well with the *RHESSI* sources.

As shown in Figure 3.2, the LT and FPs have well-defined and correlated motions, with the symbols indicating their emission centroids at different times. The white dashed straight line represents the main direction of the LT motion, which is roughly at a right angle to the solar limb. We refer to the motion along this direction as changes in altitude. The motion perpendicular to this direction might be due to asymmetry of the reconnecting loops or the LT motion along an arcade. Before the rise of the impulsive HXR emission, there is an apparent downward LT motion. This downward motion could indicate a shrinkage of newly formed loops. It may also be due to the formation of nearby sources (Krucker, Hurford, & Lin, 2003) or to projection effects should the LT source move eastward along an arcade of loops (Sato, 2001). Qualitatively similar features have been seen in several other flares (Krucker et al., 2003; Sui & Holman, 2003), suggesting that this may be a common characteristic of solar flares. However, for the remainder of the flare duration the LT source rises systematically. The apparent separation of the FP sources, whenever detectable, also increases with comparable speed. As emphasized above, this is expected in a simple continuous reconnection process that moves up to the corona, accelerating particles and energizing plasma higher up into overlying larger loops.

To analyze the FP motion quantitatively, one needs to take into account projection effects because any motion and its associated uncertainty in the east-west direction are amplified by a factor of about $\csc 77^\circ \simeq 4.4$. Motions in this direction are highly uncertain, and the motion of both FPs appears to have an east-west component. Magnetic reconnection, on the other hand, is characterized by the change in the size of newly formed loops rather than their absolute motions. Thus one may concentrate on the relative motion of the two conjugate FPs. In the insert panel of Figure 3.2, we illustrate this relative motion by fixing the S-FP at the origin of the coordinates and showing the relative locations of the N-FP. The relative motion is obviously systematic. The fact that the line tracing the location of the N-FP is not exactly aligned with the lines connecting the two FPs shows that there is another component of the relative motion introducing a small rotation of the plane containing the newly formed loop. Because this line is nearly parallel to the longitudinal line, one can ignore the projection affects. We quantify the relative motion along this line, and

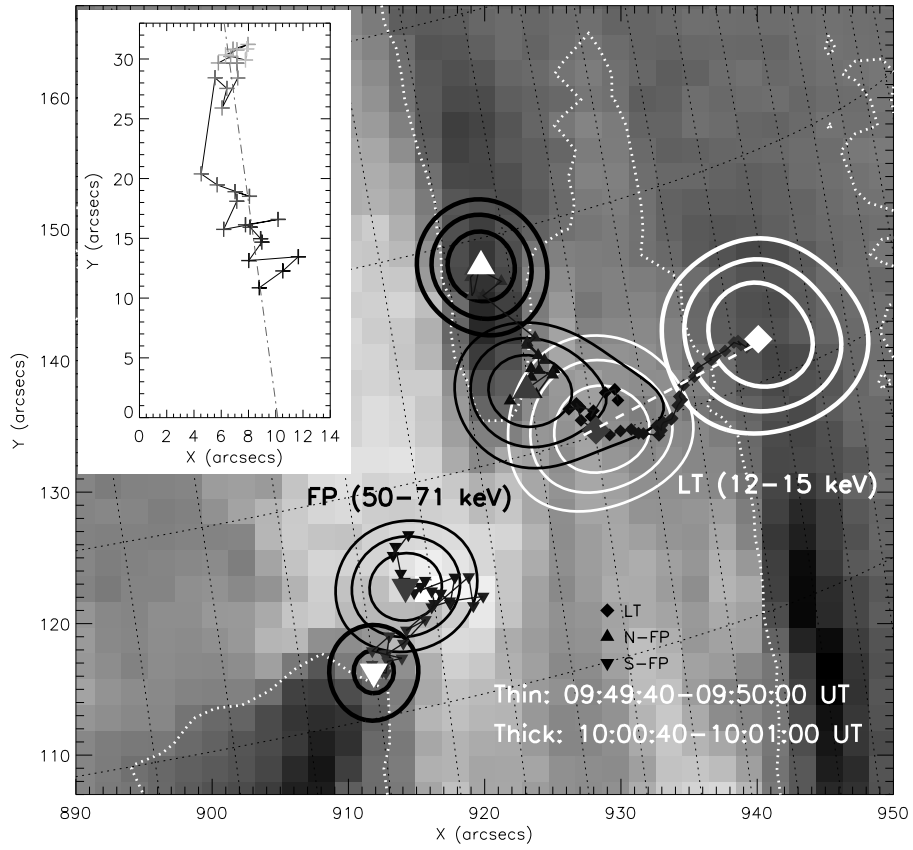

Figure 3.2: Temporal evolution of HXR source centroids, over-plotted on an MDI magnetogram (09:32:30 UT). Black line segments connect the centroids obtained from CLEAN images in successive 20 s intervals chronologically from dark (09:46:20 UT) through gray to white (10:01:00 UT). The LT (12–15 keV) centroid is the brightness-weighted source center within the 70% level contour, but each FP (50–71 keV) centroid is the peak position obtained with a 3×3 pixel parabolic fit around the brightest pixel. The white dashed straight line represents the main direction of motion of the LT source. To estimate the uncertainty in the LT centroid location, we fitted the LT data points with four straight lines within the time intervals, 09:46:20–09:49:40, 09:49:40–09:52:00, 09:52:00–09:55:20, and 09:55:20–10:01:00 UT, respectively. For each interval, following Krucker et al. (2003), the standard deviation of the offset of the data from the corresponding straight line was used as the error in the location. The insert shows the relative positions of the N-FP with respect to the S-FP, which is fixed at the origin. We attribute the motion perpendicular to the straight line to uncertainties in the locations (see text for details). Four HXR images in two time intervals, 09:49:40–09:50:00 (*inner*) and 10:00:40–10:01:00 UT (*outer*), and in two energy channels, 12–15 (*white*) and 50-71 keV (*dark*), are overplotted as contours (at 55%, 70%, 85% levels of the maximum brightness of the image), which clearly depict the LT and FPs, respectively. The centroids corresponding to these two intervals are indicated with larger symbols. The magnetogram shows the line-of-sight magnetic field in a gray scale ranging from −979 (*black*: pointing away from the observer) to +1004 Gauss (*white*). The apparent neutral lines are marked as white dotted lines [from Liu, W. et al. 2004a].

the standard deviation of the displacement (apparently) perpendicular to this line is used as an upper limit for the uncertainties of this relative motion.

Figure 3.3*b* shows this relative motion of the FPs (at 50–71 keV) along with the location of the emission centroids of the LT source in three energy bands projected onto its main direction of motion that is nearly perpendicular to the solar limb. As evident, the two motions are correlated and the two sets of data points are nearly parallel to each other indicating comparable velocities. To further investigate these motions we divide the observed flare duration into four phases: a pre-impulsive phase (before 09:48:10 UT) when there is no significant high-energy HXR emission, a rising phase (from 09:48:10 to 09:49:50 UT), a declining phase (from 09:49:50 to 09:56:50 UT), and a second active phase (from 09:56:50 to 10:01:00 UT). We then fit straight lines to each segment and determine the corresponding average velocities. The results are summarized in Table 3.1. Surprisingly, the LT velocity is highest in the declining phase, when the X-ray emission is relatively weaker (Fig. 3.3*c*). In the simplest model of reconnection of *uniform* and oppositely directed magnetic fields, one would expect the opposite correlation, i.e., a higher rate of energy release when the velocity is larger. However, this would be true if the observed HXR flux were actually proportional to the total energy release and if reconnection were indeed occurring in a uniform background plasma, neither one of which is exactly true.

Table 3.1: LT velocities and FP separation speed.

Time range	LT velocities (km/s)				FP speed(km/s)
(UT)	9-12 keV	12-15 keV	15-19 keV	19-24 keV	(50-71 keV)
09:46:20-09:48:10	-18.3 ± 3.7	-22.5 ± 4.6	-32.5 ± 4.1	-30.8 ± 4.7	— — —
09:48:10-09:49:50	3.5 ± 3.3	4.0 ± 3.0	4.7 ± 2.6	4.3 ± 2.7	29.1 ± 11.6
09:49:50-09:56:50	14.6 ± 0.4	16.5 ± 0.2	18.0 ± 0.2	20.9 ± 0.1	22.4 ± 2.5
09:56:50-10:01:00	9.3 ± 0.9	8.6 ± 0.7	6.6 ± 0.7	5.9 ± 0.5	10.4 ± 3.6

Another interesting morphological evolution is the change of the centroid of the LT source with energy. In Figure 3.4 (*left*) we show the *RHESSI* 75% contours and centroids at several energies superposed on an MDI continuum image showing sunspots. Compared with the two FPs, the LT source shows a clear and systematic displacement of the centroid of the higher energy emissions toward higher altitudes, as seen in two other flares (Sui & Holman, 2003; Gallagher et al., 2002).

To investigate what this separation of the LT centroids is related to, we looked for its correlations with other characteristics. We found an anticorrelation between the centroid separation and the high-energy (100–300 keV) count rate, which comes mainly from the FPs (3.3*d*). The continuous curve in Figure 3.4 (*right*) shows their cross-correlation function, which gives a peak correlation coefficient of -0.51 ± 0.08 with a time lag of $\Delta t = -22 \pm 39$ s. The data points (LT separation vs. HXR count rate) used for evaluating the correlation and a straight-line fit are also shown in the same figure.

3.2.2 Imaging Spectroscopy

We also analyzed the spectra of this flare. In most cases, the spatially integrated spectra from 8 to 100 keV can be fitted with a double power law (DPL) model or a thermal plus a

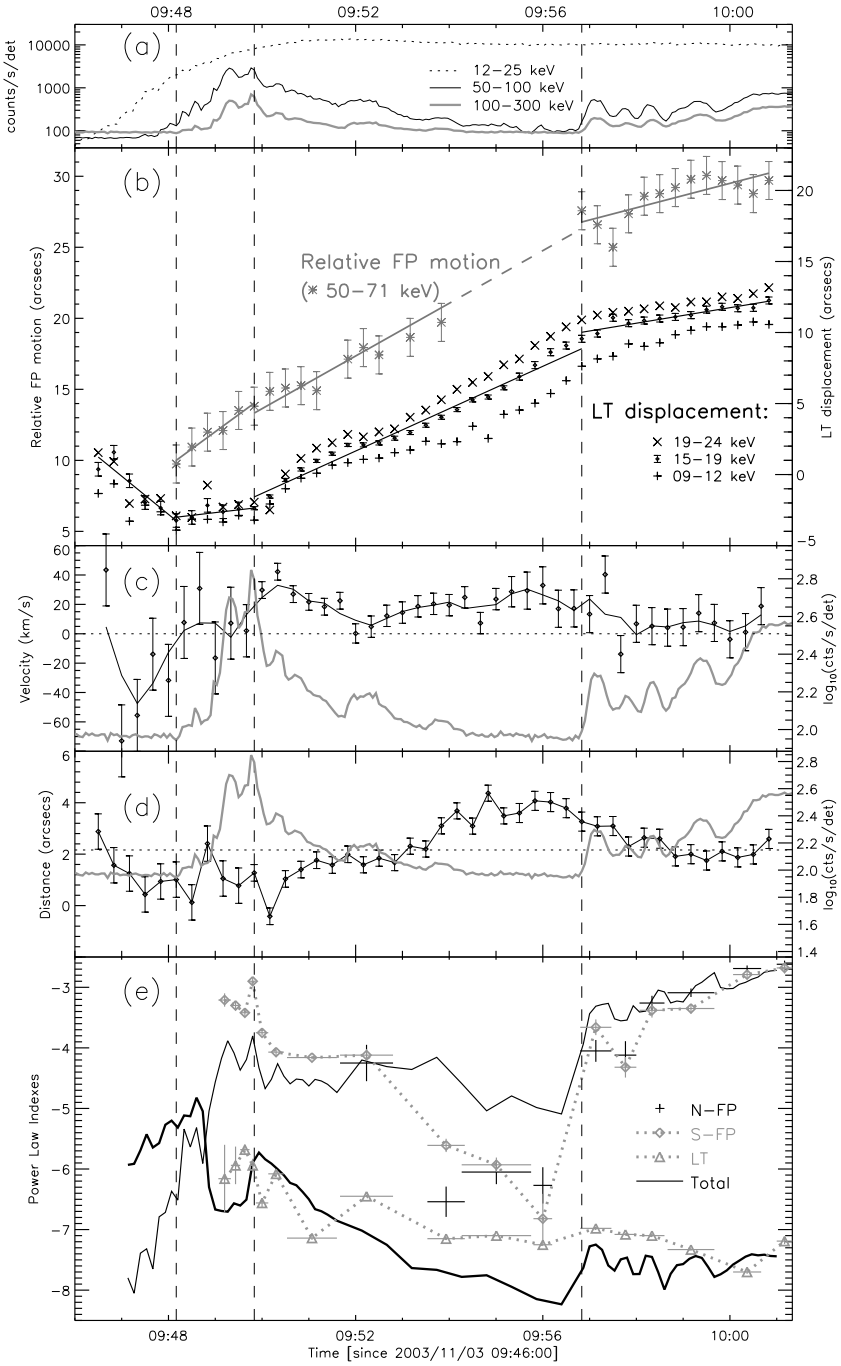

Figure 3.3: (*a*) *RHESSI* light curves. (*b*) Evolution of the displacement of the LT centroid (*right scale*) and the separation of the two FPs (*left scale*). The straight lines are fits to the data (15-19 keV for LT). The vertical dashed lines separate the four phases (see text). (*c*) LT velocity at 15–19 keV (*symbols*) and its value (*thin line*) smoothed over one minute intervals. The thick curve is the logarithmic count rate at 100–300 keV (*right scale*). (*d*) Separation of the LT centroids at 19–24 and 9–12 keV (panel *b*), together with the count rate logarithm (same as *c*), vs. time. The dotted line marks their mean. (e) Spectral indexes for various model fits. The thick and thin solid curves give the low and high energy indexes of the spatially integrated spectra. Imaging spectroscopic results are indicated by the points with 1σ vertical error bars. Horizontal error bars represent imaging integration time. [*a–d* from Liu, W. et al. 2004a].

power law (ThPL) model with similar reduced χ^2_r. The time history of the DPL parameters are shown by the solid lines in Figure 3.3*e* (The high energy index of the ThPL is nearly identical to that of the DPL). Note that during the first rising phase the spectra change from convex to concave (Holman et al., 2003), as can be seen from the intersection of the low- and high-energy indexes.

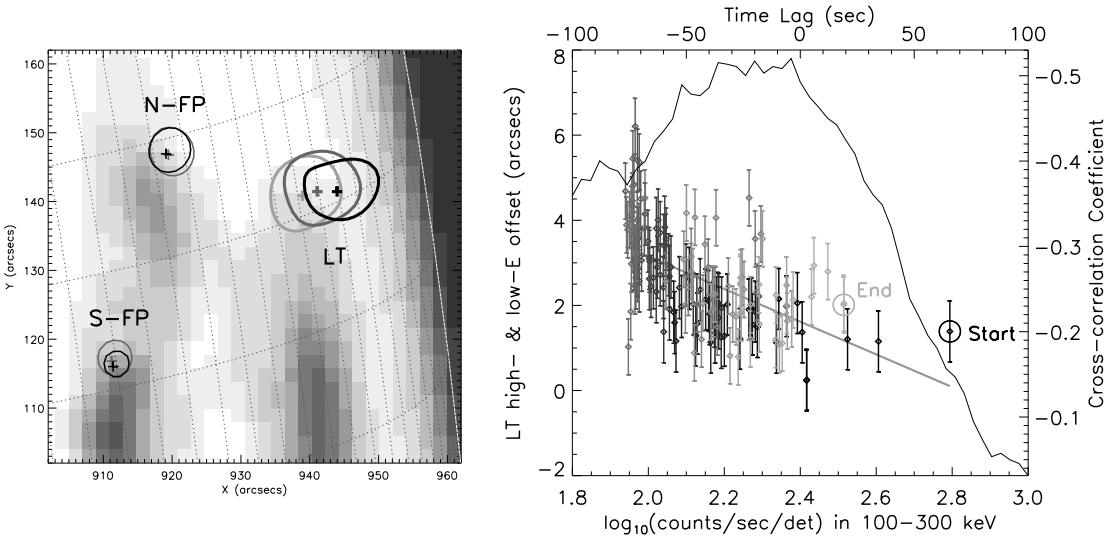

Figure 3.4: *Left: RHESSI* image contours (75%) and the corresponding brightness-weighted centroids (*plus signs*) in the interval 10:01:00–10:01:20 UT. The LT contours are for 12–14 (*light gray*), 18–21 (*gray*), and 27–31 keV (*dark gray*) and the FP contours are for 40–46 (*gray*) and 60–73 keV (*dark gray*). The background is an MDI continuum map taken at 09:36:00 UT. The dark areas inside the limb are three sunspots. *Right:* Correlation between the LT structure and the 100–300 keV (mainly FPs) light curve. The thin curve (with the top and right axis) shows the cross-correlation coefficient of the logarithm of the count rate and the separation between the 19–24 and 9–12 keV centroids of the LT source, showing a 22 ± 39 s delay relative to the light curve. The separation is similar to that shown in Fig. 3.3*d* but with a higher time resolution, obtained by imaging at a 4 s cadence (same as the light curve) with an integration time of one spacecraft spin period (~ 4 s) from 09:49:48 to 10:01:00 UT. We excluded the first two phases of the flare duration when the spatial contamination to the LT source by the N-FP is severe. The diamond symbols (with the bottom and left axis) show the LT separation vs. the logarithm of the count rate shifted by +24 s, corresponding to the peak of the correlation coefficient. The vertical error bars represent the uncertainty in the centroid separation. The darkness of the symbols represents time with the start and end point being circled. The gray thick line is a linear fit to the data with a slope of -3.84 ± 0.34 [from Liu, W. et al. 2004a].

For the purpose of imaging spectroscopy we reconstructed CLEAN images (pixel size of $1''$) with detectors 3-6 and 8 (excluding detector 7 because of its poor spectral resolution) at photon energies from 12 keV through 200 keV in 18 time intervals mostly selected at the peaks of the higher energy emission. To get the spectra of individual sources we used the component maps. For a given area, taking into account the over-sampling of the $1''$ pixel size compared to the $\sim 9''.5$ FWHM resolution (S. Krucker, private communication), the

RMS fluctuation in the residual map was used to estimate the error of the corresponding source flux. When the FPs and LT are well separated, we successfully obtained the spectra of the LT and two FP sources. Early in the event (between 09:47:48 and 09:51:37 UT) when the LT and N-FP source are partially overlapped, we first obtained the spectrum of the S-FP and the combined spectrum of the LT and N-FP. Then assuming that the two FP sources have the same spectral index and dominate at high energies (> 50 keV), we subtracted the N-FP spectrum (normalized appropriately) from the combined spectrum to obtain the LT spectrum.

In general, the spectra of the two FPs can be fitted by a single power law with very similar indexes and their fluxes are consistent within a factor of ~ 2. The LT spectrum can be fitted by a power law as well and its index is smaller than those of the FPs by > 4 units (Fig. 3.3*e*). This difference is larger than that found by Petrosian, Donaghy, & McTiernan (2002) though. On the other hand, as we have shown earlier in Chapter 2, a large difference of 3.49 between the average FP and LT spectral indexes are also found from our preliminary statistical study, which seems to be consistent with the stochastic acceleration model (Petrosian & Liu, S. 2004). (Note that the LT and FP spectra are fitted in the energy range 12-200 keV. However, the FP spectral indexes are mainly determined by data above 30 keV because data points below this energy have relatively large error bars, while most of the contribution to the LT index comes from data below 30 keV as the LT spectrum has comparably large errors above 30 keV.) There also seems to be a weak *anti-correlation* (see also Fig. 2.10) between the indexes of the LT and FP sources during the second active phase of the flare. This is not expected from simple solar flare models. Unlike other *RHESSI* flares that we have studied, in this flare a thermal model gives a poor fit to the LT spectra for most of the times (Holman et al. 2003).

The bottom panel of Figure 3.3 shows that the imaging spectroscopic results (without pileup correction which is not yet available for imaging) are roughly consistent with the spatially integrated values (which are corrected for pileup). The primary reason for the difference most likely is due to the presence of extended sources (Schmahl & Hurford, 2002) as well as some pileup effects. To investigate the pileup effect on imaging spectroscopy, we fitted the LT spectra in 12-30 keV energy range (Emslie et al., 2003), where the pileup effect is negligible and found that the power-law index changed by 10% in the worst case (livetime $\sim 77\%$) and by less than 5% at all the other times ($73\% \leq$ livetime $\leq 94\%$). The pileup correction therefore will not change the imaging spectroscopic results significantly.

3.3 Summary and Discussion

We have investigated the 2003 November 3 X3.9 flare, having a simple morphology with well-defined LT and FP sources. The high flux combined with the simple loop structure allows us to determine the spatial evolution of the LT and FP sources clearly and to compare with the simple reconnection models. Similar studies of flares have been limited to the investigation of the motion of the FPs alone (Sakao, Kosugi, & Masuda 1998; Qiu et al. 2002; Fletcher & Hudson 2002) or have dealt with complex loop structures (Krucker et al. 2003; Qiu, Lee, & Gary 2004). This has made the comparison with models more difficult. Our analysis of *RHESSI* data has yielded several new and interesting results.

1. We observe a systematic rise of the LT source and a comparable increase in the separation of the FPs as the flare proceeds. This agrees very well with the canonical solar flare model of magnetic reconnection in an inverted Y configuration. Similar behaviors have been reported previously using soft X-ray or EUV observations (Švestka et al., 1987; Tsuneta et al., 1992; Gallagher et al., 2002) during later thermal gradual phases of flares. However, these emissions are not directly related to the impulsive particle acceleration processes (Forbes & Acton, 1996).

2. The LT source seems to move more slowly during the HXR peaks than during the declining and more quiescent phases, in apparent disagreement with reconnection of *uniform* and oppositely directed field lines, where one would expect a correlation between the velocity of the LT source and the energy release rate. However, we note that the HXR flux is not a good proxy for the energy release rate, and the magnetic fields in the reconnection region are likely to be nonuniform. Stronger magnetic fields would require a smaller volume of reconnecting fields and possibly slower motion. However, in an inhomogeneous case other factors such as the geometry and Alfvén velocity variation can also come into play. This problem needs further exploration.

3. The centroid of the LT source appears to be at higher altitudes for higher photon energies. This suggests that the energy releasing process happens above the LT and that harder spectra, implying more efficient acceleration, are produced at higher altitudes. In the stochastic acceleration model by turbulence where the acceleration efficiency depends on the intensity of turbulence, this would indicate a decrease of the intensity with decreasing altitudes, presumably because of decay of turbulence away from its source at a higher altitude (Petrosian & Liu, 2004).

4. The above shift of the centroids decreases with the increase of HXR flux from the FPs. Such an anticorrelation will be difficult to produce in simple models. In the above-mentioned model, this would imply a more inhomogeneous distribution of turbulence during more active phases, because a smaller shift means a larger spatial gradient.

5. The spatially integrated spectra are fitted equally well with a double power-law model and a thermal plus power-law model.

6. The imaging spectroscopy study suggests that the LT and FP sources could be purely nonthermal. In the second active phase of the flare, there appears to be an anti-correlation between spectral indexes of the LT and FP sources and their difference can exceed 4.

Another possible explanation, in regard to No. 4 mentioned above, concerns the interplay of the heating/acceleration and cooling processes. Studies of the evolution of loops in the gradual phase indicate that cooling of the plasma confined within closed loops plays an important role in determining the observed emission morphology (Forbes & Acton 1996). If cooling is also important in the impulsive phase, one would expect that loops forming earlier have lower plasma temperatures and contribute mainly to emission at lower energies. Then the motions of the emission centroids at lower energies will be dominated by the cooling process. The motions of centroids at higher energies, however, are presumably determined

by the heating/acceleration process, a direct consequence of reconnection. When higher energy sources slow down due to the increase of reconnecting magnetic fields as discussed above, the apparent velocities of lower energy sources do not change significantly until their centroids are determined by emission from hotter plasmas at the reconnection site. The sudden decrease of the 19-24 keV centroid velocity and the relatively smooth transition of the 9-12 keV centroid motion during the onset of the second HXR burst (Fig. 3.3*b*) and the delay of the LT centroid separation relative to the light curve (Fig. 3.4, *right*) seem to support such a scenario.

A more detailed analysis of this flare including imaging spectroscopy and quantitative comparison with theoretical models will be needed to shed light on the observations presented here and distinguish between the possibilities discussed above.